Needle Detection in Three-Dimensional Ultrasound Imaging

Pourtaherian, Arash

Award date:
2013

Awarding institution:
Eindhoven University of Technology

Technische Universiteit
Eindhoven
University of Technology

Department of Electrical Engineering

Den Dolech 2, 5612 AZ Eindhoven
P.O. Box 513, 5600 MB Eindhoven
The Netherlands
http://w3.ele.tue.nl/nl/

Series title:
Master graduation paper,
Electrical Engineering

Commissioned by Professor:
prof. dr. ir. P.H.N. de With

Group / Chair:
SPS / VCA

Date of final presentation:
August 23, 2013

Report number:

1224

Needle Detection in Three-Dimensional Ultrasound Imaging

by

Author: Arash Pourtaherian

Internal supervisors:
prof. dr. ir. P.H.N. de With, prof. dr. H.H.M. Korsten, and dr. S. Zinger

External supervisor: dr. ir. N. Mihajlovic

Needle Detection in Three-Dimensional Ultrasound Imaging

Arash Pourtaherian
Video Coding and Architectures Research Group, Signal Processing Systems
Department of Electrical Engineering, Eindhoven University of Technology

***Abstract*—During medical interventions with needles, it is important to visualize the needle position and its tip with respect to important structures in the patient's body. Ultrasound (US) is one of the most popular imaging modalities for such interventions. However, capturing the full-length needle during the intervention procedure is challenging with a two-dimensional (2D) ultrasound imaging modality. For this reason, a highly-skilled physician is needed to perform needle interventions efficiently under US guidance to optimize intervention success. In this work, we propose a novel image-based needle detection technique using a three-dimensional (3D) imaging modality. We extract 2D cross-sections from a 3D volume in order to visualize the full-length needle and its tip. The needle detection algorithm is based on supervised model-based learning, which exploits needle-like structures in the volume. Evaluation of our system shows a high detection score of finding appropriate 2D cross-sections that contain the needle and its tip. This application can support physicians during medical interventions with needles and be an aid in minimizing complications.**

***Index Terms*—needle detection, three-dimensional ultrasound imaging, interventional guidance, 3D Gabor transformation**

I. Introduction

MEDICAL interventions with needles have a wide variety of applications in medical diagnostics and treatments. For example, in breast biopsy, prostate brachytherapy, radio frequency ablation and epidural anesthesia, a needle is used to access remote targets in the patient's body to take tissue samples and to deliver medicine or electric energy. Visualization of the needle and its tip is helpful and in many cases vital. This can help physicians to minimize risks during various interventions, lower the amount of medicine and shorten patient's recovery time. Therefore, in most cases, medical imaging technologies are utilized to locate and guide the needle inside the patient's body [1]–[3]. Ultrasound (US) is one of the most popular imaging modalities for such interventions because it uses non-ionizing radiations and provides real-time images at affordable costs.

Under Two-Dimensional (2D) US guidance, capturing the needle and its tip during the intervention is challenging. Any hand motion may cause parts of the needle to be excluded from the image and lead to errors in locating the tip of the needle. As an alternative, Three-Dimensional (3D) US, can overcome 2D US limitations in image-guided interventions [4]. However, 3D US imaging requires computer-aided techniques for appropriate analysis and visualization of 3D volumes. Detecting the needle and enhancing its visibility will allow needle operators to perform interventions more accurately. Furthermore, assuring that the needle is fully visible for the physician will minimize the risk and duration of an intervention.

Needle detection approaches in US images can be divided into image-based detection algorithms [5] and external tracking systems. Examples of the external tracking are mechanical [6], electromagnetic (EM) [7] and optical tracking [8] systems. In mechanical systems, a robotic arm is used to perform the intervention, which provides initial knowledge of the exact needle position. In electromagnetic and optical tracking, a tracking device (position sensor) is attached to the US probe and its location is registered to the US image coordinates. Because of the limitations of the external tracking systems, such as large setup, limited accuracy and the increased costs, they are not commonly used. Therefore, image-based detection algorithms are more attractive for such applications. In order to improve the needle visibility and support image-based detection techniques, modifying the signal generation by adaptive beam steering [9] has been proposed. Moreover, mechanical scoring and chemical coating of the needle increases its brightness in US images [10]. Nevertheless, because of the limitations of the US imaging, such as the intrinsic low signal-to-noise ratio, presence of imaging artifacts, anisotropic nature of the images, etc., most of the image-based needle detection studies fail to propose a generic solution for detection in diverse environments (Section II).

In this work, we propose an efficient image processing concept for needle detection in 3D US without employing any supporting external systems. Our needle detection algorithm enhances and normalizes the images and exploits the needle-like structures in the 3D US volume. We present the following contributions: (1) normalization of the needle visibility by applying adaptive histogram equalization; (2) novel needle detection technique using a supervised model-based approach; (3) 3D Gabor transformation as feature extraction to exploit needle-like structures; (4) visualization of the needle and its tip with 2D cross-sections of the volume.

II. Related Work

Needle detection techniques mainly consist of the following stages. First, US images are pre-processed to remove noise and maintain the desired quality for applying detection algorithms (Section II-A). Second, the image-based needle detection concentrates on extracting relevant information required for deriving the needle position and its orientation (Section II-B). Third, needle orientation and position is computed

Table I: Overview of image-based needle detection techniques

Algorithmic Step	Technique		Methodology	Remarks
Image restoration and enhancement	Deconvolution (restoration)		Counteracts PSF	⊕ Improves resolution ⊖ Complex to estimate PSF
	Filtering (enhancement)	First order statistics	Mean and/or median filtering	⊕ Computationally efficient
		Adaptive	Smooth only the noisy regions	⊕ Unaltered non-noisy regions
		Aniosotropic diffusion	Based on heat distribution	⊕ Edge enhancement
		Wavelet transform	Reduce wavelet coefficients of noise	⊖ Poor speckle reduction
		Second-order derivative of Gaussian		⊕ Preserving the needle
Relevant information extraction	Using *a priori* knowledge	EM tracking sensor	Approximate position is known	⊕ Increase the efficiency ⊖ External tracking needed
		Coarse-fine search	Search at two resolution stages	⊕ Increase the efficiency
		Manually annotations		⊕ Limit false detections ⊖ Requires human interaction
	Projection of 3D on 2D planes	Ray-casting	Based on a volume rendering	⊖ Details can be lost
		Averaging		⊖ Details can be lost
	Thresholding		Transform to a binary image	⊕ Complexity reduction
	Edge detection		Detecting the edges in the image	⊕ Candidate points reduction
	Line filtering		Detecting lines in the image	⊕ Candidate points reduction
	Background subtraction		Integral difference of frames Comparing with the needle movement	⊕ Similar regions elimination ⊖ Not applicable to still images
	Modeling US background		Select frames with stationary needle	⊕ Complexity reduction
Needle orientation and position detection	2D detection	Model fitting	Fit a line or tube using PCA	⊖ Poor performance on US
		Active contours	Deforming by forces of features	⊖ Noise sensitive
		Hough transform	map points to a parameter space	⊖ Computationally complex
		Randomized Hough	Select random points to map	⊕ Can be real-time
		Gabor transform	Searches in different orientations	⊕ Searches for a fixed width
	Parallel Integral Projection (PIP)		Localize tool's axis by observing the projection along multiple axis	⊕ No need for line detection ⊖ Computationally complex
	RANSAC		Estimate tool's axis	⊕ Computationally fast ⊖ Large random errors
	Needle tracking		Correlate detections over subsequent frames	⊕ Eliminate false detections

in a 3D volume or a 2D plane (Section II-C). Image-based needle detection techniques are summarized in Table I.

A. Image Restoration and Enhancement

The quality of US images is degraded due to many types of artifacts. Although techniques are developed to enhance the US image and reduce the noise, they are limited by the intrinsic quality of the acquired data and related conditions. For example, a shadowed region cannot be restored since the data is not present, or the PSF and reverberation artifacts may obscure image details. The Point Spread Function (PSF), also known as the resolution cell of the system, is caused by diffraction of the US signals and convolves with the reflected wave, thereby resulting in blurred images [11]. Speckle noise is a result of scattered signals reflected from targets below the pulse resolution and appears as intensity fluctuations in the image [11].

Generally, two main techniques, i.e. filtering and deconvolution, exist to improve the quality of US images after they have been generated and digitized. Filtering aims at increasing the SNR of the image, while deconvolution improves image resolution [12]. Deconvolution techniques estimate the PSF to counteract the diffraction degradation [13]. For filtering, several techniques for speckle reduction in US images have been proposed and applied. Adaptive filtering [14] and anisotropic diffusion filters [15], have shown to be suitable for smoothing homogenous regions while retaining edges [16]. A bank of modified Gabor filters is applied to the 2D radio-frequency data [17], to reduce the speckle and enhance structure information. The wavelet transform filter is applied to US images, followed by the speckle noise wavelet shrinkage [18]. This has proven to give a poor performance [16] and the best choice is claimed to be the first-order statistics filter. In a speckle reduction comparison study [19], an oriented speckle anisotropic diffusion filter [20] has given optimal filtering for speckle suppression, edge preservation and computational efficiency.

In a needle detection study, a median filter is used for speckle removal [21], which was causing the needle to appear broken into a series of many disconnected parts and not suitable for further processing. In its follow-up study [22], a mean filtering is used yielding more robustness. A more advanced method is based on an anisotropic diffusion [23] to filter homogenous regions and still preserve the needle. The resulting image is passed through a contrast enhancing spatial-domain filter, and a non-binary morphological opening operation. A more recent study [24], applies rotated versions of the second-order derivative of a Gaussian filter to keep the tubular shape of the needle in different directions, while smoothing other structures in the image.

B. Relevant Information Extraction

A popular approach to limit the computational complexity is to use *a-priori* knowledge of the approximate orientation, position or thickness of the needle, to limit the false detections [22], [24], [25] or to crop the informative volume [26]–

[30]. The approximate position of a needle can be also derived from an EM tracking sensor integrated in the needle [24], [25], from the coarse-fine search strategy [26]–[28], [30], or by manually annotating the needle's region [22], [29]. The coarse-fine search strategy is first introduced for 2D US [30] and later applied to the 3D US [27], [28]. This technique searches for the needle in two stages: a coarse stage in a low-resolution image to obtain the approximate position, and a fine stage to obtain a high spatial accuracy.

Different techniques for 2D US images have been developed for more than a decade and have shown promising results. As 3D US systems have become more available, 2D detection techniques have been adapted for implementation in 3D US images. First attempts are based on projecting the 3D volume onto two orthogonal planes and identifying the needle on the two 2D images. Projection of the 3D volume is mostly done by averaging and ray-casting, which is traditionally used in volume rendering. Later studies have modified the projection technique to increase the speed and accuracy of the detection [23], [26].

A popular method of candidate pixel (voxel) extraction is thresholding, which is also effective in reducing the computational complexity [5], [6], [27]–[36]. Edge detection [21], [22], line filtering [37] and background subtraction [24], are used to limit the candidate needle points. In a more advanced technique, the needle region is identified with an "integral difference of frames", assuming that the movement pattern of a needle is different from other regions [38]. A similar concept of modeling the US video background is used in addition to selecting the frames with a stationary needle only [24].

C. Needle Orientation and Position Detection

In early needle detection studies, flood-filling [30] and Hough transformation [39] are used to detect the needle in the 2D US image. Later, the thresholded image is used to detect the needle by fitting a line [31] or a tubular model using Principle Component Analysis (PCA) [5]. However, PCA-based methods fail when the needle appears discontinuous, which happens regularly in US images. A level-set shape-based segmentation, also known as snake model, is used to model the shape of the needles in 2D [38] and later in 3D Transrectal US [29]. Shape-based segmentation consists of active contours that deform based on a partial differential equation caused by the forces of image features. An appealing technique to localize the needle in 2D US images is the Hough transform, which detects lines by mapping all points in the image to a parameter space. Modified versions of the Hough transform are proposed to detect other objects and curved needles [22].

In more recent approaches of needle detection in 3D US images, the representation of a straight line in 3D proposed by Roberts [40] is adapted to directly apply the Hough transform in 3D US images [27], [28], [32]. Randomized Hough Transform (RHT) is used [28] to decrease the computational complexity of the needle detection. The Parallel Integral Projection (PIP), that is a generalized form of the 3D Radon transform [41], is used to localize the instrument's axis by maximizing the projection of the image along multiple lines [42], or along a curve [25]. Since PIP-based techniques are computationally complex, a fast implementation on a Graphics Processing Unit (GPU) is proposed [42] to achieve real-time performance. A hierarchical mesh-grid search algorithm is applied to decrease the complexity of the technique [43]. However, in its follow-up study [34], it is claimed that in addition to the computational complexity of PIP, it is not robust for localizing very thin objects in a cluttered background. Therefore, the authors propose to utilize a model-fitting approach, based on RANdom SAmple Consecsus (RANSAC) [44]. RANSAC has been used earlier followed by least square curve fitting for localizing the curvilinear object in 3D US images [33]. In the succeeding studies [34], [35], surgical tool localization is studied by estimating its axis with a RANSAC search algorithm, and locally optimized for a more accurate detection. Although RANSAC-based localization methods are claimed to be fast and accurate compared to the RHT-based and PIP-based methods, depending on the experimental settings they can introduce large random errors in the result. A Kalman filter is added to avoid such errors by estimating the tool's position [36], which is claimed to add more stability to the detection algorithm. Prior to this study [45], a Gabor filter that was traditionally used for image enhancement is utilized as line detector with a fixed thickness to reveal the needle structures in the US images.

After the needle axis is identified in 3D, the tip of the needle can be recognized, which is commonly done by finding the farthest pixel along the needle's axis with an intensity above a threshold [31], [34], [43]. Recently, it is proposed to track the needle over subsequent frames (US images) to eliminate the false detections of the regions with similar appearance to the needle [38]. A more advanced approach uses a Kalman filter to estimate and track the tip of the needle [36], in order to avoid random errors of RANSAC.

III. Methodology

The work in this thesis is divided into two different needle-detection approaches, as depicted in Figure 1. In both approaches, the 3D US volume is acquired from a needle-insertion procedure and then, the volume is pre-processed for enhancement and normalization. Next, needle detection algorithms are performed for projection-based and the proposed Gabor-based techniques. Finally, 2D cross-sections of the volume containing the needle and its tip, are visualized to the operator.

A. Ultrasound Volume Acquisition

A 2D US image is acquired by transmitting an array of pressure (acoustic) waves through the patient's body and converting the reflected waves into electrical signals. Pressure waves are created by exciting a large number of piezoelectric crystals placed on a line (linear transducer) or a convex curve (sector transducer). Regions with higher acoustic impedance appear as high intensity pixels in the US image.

In order to acquire 3D volumes of US data, two types of transducers can be used: steered transducers and matrix transducers. In steered transducers, a linear or sector transducer is

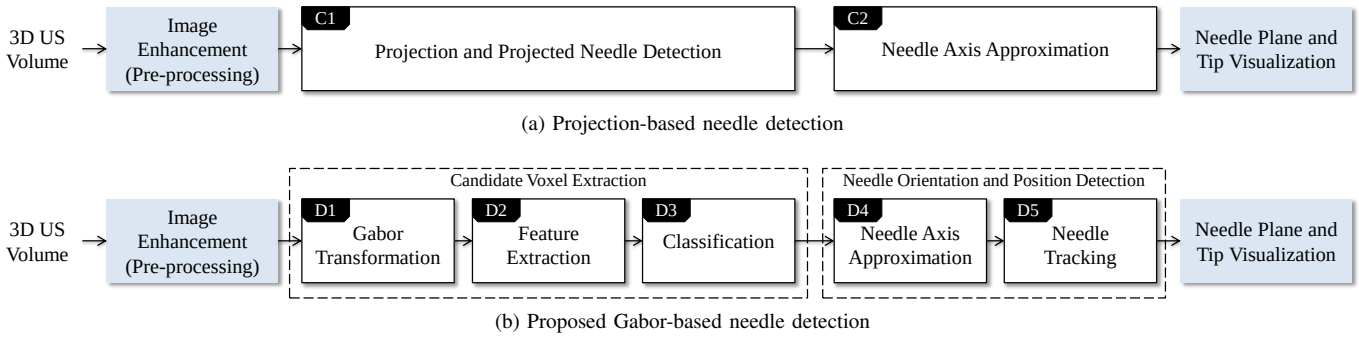

(a) Projection-based needle detection

(b) Proposed Gabor-based needle detection

Figure 1: Block diagrams of the implemented needle detection techniques

tilted or shifted to acquire a series of 2D images, forming a 3D volume. Steering is done using a motor to provide quantifiable volumetric data. In matrix transducers, piezoelectric crystals are arranged in a rectangular grid, which allows for 2D beam steering and results in a 3D volumetric dataset.

In this work, several sets of 3D US volumes were acquired with an iU22 xMATRIX Ultrasound system[1] using a VL13-5 motorized 3D broadband linear array transducer applied to chicken breast phantoms.

The coordinate system of the acquired volume is defined relative to the transducer position, as shown in Figure 2. The direction of orientation pointer corresponds with the negative y direction of the coordinate system. A line in 3D can be described with a point and a direction vector [40]. Therefore, we define the needle axis in the 3D volume to be represented by four parameters (θ, ϕ, x_0, z_0) and describe it in the Field of View (FOV) by:

$$\begin{bmatrix} x \\ y \\ z \end{bmatrix} = \begin{bmatrix} \sin\theta\cos\phi \\ \cos\theta\cos\phi \\ \sin\phi \end{bmatrix} t + \begin{bmatrix} x_0 \\ 0 \\ z_0 \end{bmatrix}, \qquad (1)$$

where θ and ϕ are the azimuth and elevation angles of the needle, respectively, and x_0 and z_0 are the coordinates of the needle in the XOZ plane (at $y = 0$).

B. Image Enhancement (Pre-processing)

In general, raw acquired US images need to be pre-processed prior to any automated analysis. Since the US images are formed from the interpretation of the reflected acoustic waves and modulated by user-controlled depth gain settings, they represent a highly anisotropic and position-dependent information. As reported also in needle-insertion procedures, the visibility of the needle is decreasing linearly with steeper insertion angles [46]. Therefore, at the pre-processing stage, in addition to the speckle reduction, needle visibility should be improved as much as possible.

The 3D US volume can be decomposed into a series of parallel 2D images (frames). In this stage, image enhancement techniques are applied to each individual frame, ignoring their temporal relation for simplicity. In order to minimize the brightness variations, a temporal median filter calculates a background model of the volume and it is subtracted from each frame. Then, successive iterations of a spatial median filter are applied to each frame to reduce the speckle noise. The last step is to normalize the visibility of structures (including the needle), based on the Contrast Limited Adaptive Histogram Equalization technique (CLAHE) [47]. We have used a block-based version of this algorithm in MATLAB, which performs a local histogram equalization with a preset maximum contrast β. For the grayscale mapping function, we have chosen a uniform histogram distribution. The final value of each pixel is obtained by performing bilinear interpolation between mapping functions of neighboring blocks.

C. Projection-Based Needle Detection

Among the approaches for detecting the needle axis in 3D, projecting the volume to 2D planes is well investigated, which has been shown to reduce the computational complexity and to be relatively accurate. In this approach, the 3D volume is projected on at least two planes and the needle is detected in each 2D projection image. The 3D volume is projected along the viewing direction first and the second projection is determined after detecting the needle in the first projection image.

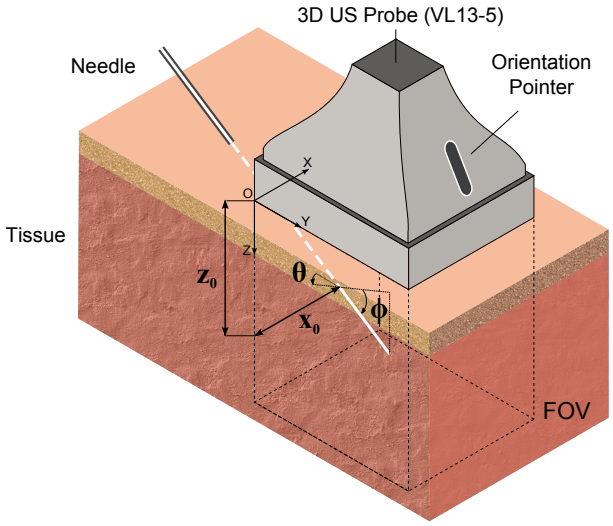

Figure 2: Coordinate system of the acquired volume, where the origin is at the top of the tissue (assume US transducer to be transparent)

[1]Commercially available from Philips Electronics.

1) Projection and Projected Needle Detection: Projecting the 3D volume by averaging the voxel values along parallel lines may suppress the needle or parts of it. Ray-casting is another popular choice, in which the voxels that are closer to the projection plane have greater influence in the resulting image. In this study, voxels with the maximum intensity are projected to preserve the voxel values corresponding to the needle. In the projected image, we detect large intensity changes using the Prewitt operator, and apply the Hough transform to detect the linear structures.

2) Needle Axis Approximation: A line can be described in the 3D volume with a cross-section of two planes. We define the first plane from the detected needle in the previous step. Then, the second plane can be defined by a second projection of the 3D volume, which is not parallel to the first. However, the second plane can also be described as the planar section of the volume along the first detected plane. Figure 3 illustrates a planar section of the 3D volume achieved by interpolating the volume along the first detected plane. As the needle should be the only bright linear object in the cross-sectional image, it is clearly visible and its axis can be detected with simple image-processing techniques, such as thresholding. In order to omit the false detections, we compare the properties of each region to the physical properties of the needle, which is long and narrow. For this reason, we fit ellipsoid blobs on each region and compare the length of the major axis to the minor axis. The needle axis can be described as the cross-section of the two detected planes in 3D (see Figure 3).

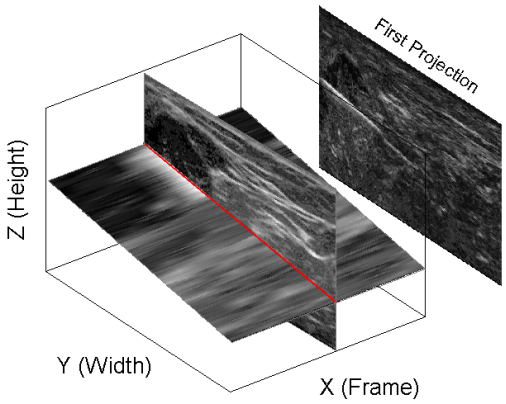

Figure 3: Projection-based needle detection: cross-section of the two planes containing the needle and the first projection

D. Gabor-Based Needle Detection

Candidate Voxel Extraction: In the majority of 3D US volumes acquired from a human body, multiple regions can exist with similar brightness and comparable structure of the needle, caused by e.g. veins, nerves, or mass. These regions can cause ambiguity in detecting the needle for common segmentation techniques. Therefore, we propose to employ a discriminative model of the needle using Gabor transformations. Gabor functions, which are shown to be good models of the object recognition path in the primate visual cortex [48] are used to extract visual features of each voxel in the 3D US volume. Voxels or groups of voxels are classified into needle/non-needle classes with a discriminative classification of the corresponding extracted features to form a set of candidate voxels. We provide detailed descriptions in Sections III-D1, III-D2 and III-D3.

1) Gabor Transformation: A signal or an image is sometimes more conveniently described in the frequency domain, instead of time or spatial domain, which can be particularly beneficial for further processing. As a first benefit, describing the volume in the frequency domain reveals dimensions of objects in different orientations, which is convenient in distinguishing the needle from other regions in the 3D US volume. The Gabor transform can represent signals simultaneously in time and frequency using elementary functions. Unlike the Fourier transform that represents a *global* frequency spectrum, the Gabor transform represents *local* distribution of the energy as a function of frequency. The 2D and 3D generalizations of Gabor elementary functions have been widely applied in image processing as filters in order to obtain the Gabor transform of the image or volume. The popularity of the Gabor transform in computer vision is illustrated by its applications in edge and line detection, texture classification, motion analysis and object recognition. A 3D Gabor filter is a complex sinusoidal plane wave modulated by a Gaussian envelope and can be defined as in Equation (2a), where λ is the wavelength of the plane wave, θ and ϕ are the clockwise azimuth and elevation rotation of the Gabor filter, respectively, ψ is the phase offset of the sinusoidal plane wave, γ_x and γ_y are the spatial aspect ratio of the envelope, σ is the standard deviation of the Gaussian envelope and b is the half-response spatial-frequency

$$g\left(x,y,z;\sigma,\gamma_x,\gamma_y,\theta,\phi,\psi\right) = \underbrace{\exp\left(-\frac{\gamma_x^2 x_r^2+\gamma_y^2 y_r^2+z_r^2}{2\sigma^2}\right)}_{\text{Gaussian Envelope}} \underbrace{\exp\left(j2\pi\frac{x_r}{\lambda}+\psi_x\right)\exp\left(j2\pi\frac{z_r}{\lambda}+\psi_z\right)}_{\text{Sinusoids}}, \tag{2a}$$

$$\begin{bmatrix} x_r \\ y_r \\ z_r \end{bmatrix} = \begin{bmatrix} \cos\theta & \cos\phi\sin\theta & \sin\phi\sin\theta \\ -\sin\theta & \cos\phi\cos\theta & \sin\phi\cos\theta \\ 0 & -\sin\phi & \cos\phi \end{bmatrix} \begin{bmatrix} x \\ y \\ z \end{bmatrix}, \tag{2b}$$

$$\frac{\sigma}{\lambda} = \frac{1}{\pi}\sqrt{\frac{\ln 2}{2}}\frac{2^b+1}{2^b-1}, \tag{2c}$$

bandwidth of the Gabor filter in octaves. The value of σ can be specified through the bandwidth b using Equation (2c). The normalized response of a Gabor filter with a particular position, size, orientation and symmetry can be calculated for a 3D volume ξ using the convolution in Equation (3) based on the 2D response presented in [49], which is specified by:

$$r_{\xi}(x,y,z) = \frac{\gamma_x \gamma_y}{\left(\sigma\sqrt{2\pi}\right)^3} \left| g(x,y,z) * \xi(x,y,z) \right|. \quad (3)$$

For simplicity, we use $g(x,y,z)$ instead of the term $g(x,y,z;\sigma,\gamma_x,\gamma_y,\theta,\phi,\psi)$. The complexity of Gabor filters is discussed in Appendix A.

2) Feature Extraction: Gabor filters are known to be good models of cortical *simple* cells [48] and can be used as feature extractors at each location, orientation and frequency with a controllable effective spatial area for object recognition [50]. Serre *et al.* [51] have investigated the correspondence of the Gabor transformation with *complex* cells along the ventral stream of visual cortex. Responses of Gabor filters are sub-sampled spatially in the volume by means of a maximum operation (max function) to obtain responses corresponding to the complex cells:

$$r_C(x,y,z) = \max_{\substack{x'\in[x-w_s;x+w_s]\\ y'\in[y-w_s;y+w_s]\\ z'\in[z-w_s;z+w_s]}} \left[r_{\xi}(x',y',z') \right], \quad (4)$$

where r_C represents Gabor response corresponding to the complex cortex cells and w_s is the sub-sampling window size. Normalized responses for different θ and ϕ form an information diagram, which represents the dimensions of the object in different orientations. If a response diagram shows all values of r_C from Equation (4), then $R(a,b)$ will be the response at position a,b in the diagram. In order to form rotational invariant features, we propose shifting and flipping the response diagram horizontally and vertically, such that the maximum response is always located at the center of the diagram. We require that the following inequalities hold:

$$R\left(\left\lceil\tfrac{N_H}{2}\right\rceil - 1, \left\lceil\tfrac{N_V}{2}\right\rceil\right) < R\left(\left\lceil\tfrac{N_H}{2}\right\rceil + 1, \left\lceil\tfrac{N_V}{2}\right\rceil\right), \quad (5a)$$

$$R\left(\left\lceil\tfrac{N_H}{2}\right\rceil, \left\lceil\tfrac{N_V}{2}\right\rceil - 1\right) < R\left(\left\lceil\tfrac{N_H}{2}\right\rceil, \left\lceil\tfrac{N_V}{2}\right\rceil + 1\right). \quad (5b)$$

Here, N_H and N_V are number of horizontal and vertical elements of response diagram R. The response diagram of each voxel forms a feature vector $\boldsymbol{X}_{1\times F}$, where F is the total number of azimuth and elevation angles of the Gabor filter bank. Gabor filters are designed to be sensitive to needle structures with different orientations. The needle appears as a long straight bright high-frequency change in the volume. Therefore, we set $\gamma_x = 1$, $\gamma_y = \frac{1}{40}$, $\lambda = 0.8$, $\theta = \{-30,-15,0,15,30\}$ and $\phi = \{-30,-15,0,15,30\}$.

3) Classification: A classifier is trained to model the discriminative information between the voxels belonging to the needle and other regions. We use a basic Linear Discriminant Analysis (LDA), also known as Fisher LDA, and show that it is computationally efficient and sufficiently accurate for extracting candidate needle voxels. In the Fisher LDA, data is assumed to have a Gaussian mixture distribution with the same covariance matrix for each class. Given an observation $\mathbf{x}$ and a number of classes K, the predicted classification $\hat{\mathbf{y}}$ is derived by minimizing the expected classification cost, giving

$$\hat{\mathbf{y}} = \arg\min \sum_{k=1}^{K} \hat{P}(k|\mathbf{x})\, C(\mathbf{y}|k), \quad (6)$$

where $C(\mathbf{y}|k)$ is the cost of miss-classification and $\hat{P}(k|\mathbf{x})$ is the posterior probability, which is a product of prior probability and the multivariate normal density. Assuming class mean μ_k and covariance matrix $\boldsymbol{\Sigma}$, the posterior probability at $\mathbf{x}$ is:

$$\hat{P}(k|\mathbf{x}) = \frac{P(\mathbf{x}|k)\,P(k)}{P(\mathbf{x})}, \quad (7a)$$

$$P(\mathbf{x}|k) = \frac{1}{\sqrt{2\pi\,|\boldsymbol{\Sigma}|}} \exp\left(-\frac{1}{2}(\mathbf{x}-\mu_k)^T \boldsymbol{\Sigma}^{-1}(\mathbf{x}-\mu_k)\right), \quad (7b)$$

where $P(k)$ is the prior probability of class k, and $P(\mathbf{x})$ is the normalization constant. This classifier can be constructed using labeled observations $\mathbf{x}_1,\ldots,\mathbf{x}_N$ and a binary class membership matrix $\mathbf{M}_{N\times K}$, where $M_{nk} = 1$ if and only if the observation n is from class k. The estimate of class mean and covariance matrix of classifier (6) is calculated from:

$$\hat{\mu}_k = \frac{\sum_{n=1}^{N} M_{nk}\mathbf{x}_n}{\sum_{n=1}^{N} M_{nk}}, \quad (8a)$$

$$\hat{\boldsymbol{\Sigma}} = \frac{\sum_{n=1}^{N}\sum_{k=1}^{K} M_{nk}(\mathbf{x}_n - \hat{\mu}_k)(\mathbf{x}_n - \hat{\mu}_k)^T}{N-K}, \quad (8b)$$

where N is the total number of training observations.

Needle Orientation and Position Detection: A model of the needle should fit with the candidate voxels. In needle insertion procedures, a popular technique is to avoid the needle to bend. As a result, the needle appears as a straight line with a fixed width in the 3D US volume. Fitting a line in a 3D point cloud is a relatively easy task. However, presence of the outliers among the needle candidate voxels decreases the accuracy and reliability of the line fitting. We propose a robust linear model-fitting approach, which first detects a set of inlier voxels and then fits a linear model with the inlier voxels (Section III-D4). Furthermore, we propose a local needle tracking stage, which can be applied individually for tracking the needle in the subsequent acquisitions. This stage can be also employed to increase the accuracy of the approximation (Section III-D5).

4) Needle Axis Approximation: Misclassified voxels can be divided into three categories: (1) voxels in the vicinity of the volume borders detected due to the sudden change of the intensity, (2) scattered voxels in the volume that do not belong to any structures and (3) voxels belonging to structures that resemble the needle appearance in a small region. We propose to omit each category of the outliers based on their properties.

Since positioning the needle to be reasonably distant from the volume borders is an easy task and a usual practice for operators, we assume the voxels at the distance d_b or closer to the borders to be ignored. Needle appearance in the volume is constructed from a series of voxels. Therefore, scattered voxels in the volume can be omitted by examining the size and shape of the blobs fitted on the detected voxels. Some

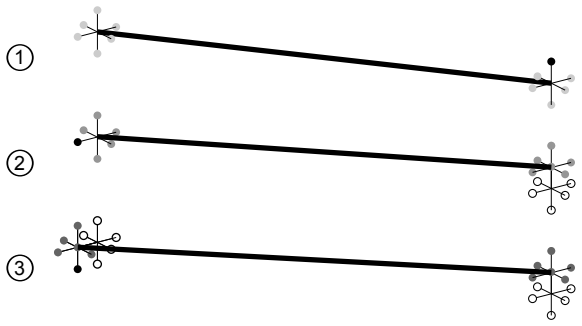

Figure 4: Example of gradient descent search pattern for three iterations, black dots indicate the locations with minimal error, gray dots indicate the search points

structures inside the body may resemble parts of the needle in a small neighborhood. We propose to detect the region, which resembles the longest straight needle as the set of inlier voxels. This is done by means of RANSAC, which detects the model with the maximum fitted voxels. If the Euclidean distance of a voxel to a model is less than ϵ, the voxel is considered to be fitting with the model.

A linear model is fitted through the set of inlier voxels using a linear least squares minimization method. Given two points on the needle in the 3D volume, the needle parameters are approximated from Equation (1).

5) Needle Tracking: Over subsequent US acquisitions, the needle movement is limited and it can be tracked from its approximate position in the previous acquisition. We propose a tracking algorithm, which locally searches for the axis with the brightest voxels. Therefore, we apply a gradient descent search algorithm for needle tracking. The introduced technique searches for the axis that locally minimizes the detection error function, specified by:

$$E(\ell) = 255 - \frac{1}{L} \sum_{x,y,z \in \ell} \xi(x,y,z), \tag{9}$$

where $0 \leq \xi \leq 255$ and L is the length of the line ℓ in voxels. At each iteration, the average intensity values on the axis are calculated for alternative positions of axis ends. Then, one of the ends is displaced by one voxel towards the lowest detection error until it converges. Here, gradient descent search is carried out with a small diamond pattern of one voxel side. Figure 4 shows an example of three gradient descent iterations to find the axis with the highest intensity values.

Moreover, the tracking stage can be applied to decrease the error of the axis approximation stage, which is limited due to the spatial blurring and sub-sampling of Gabor transformation.

E. Needle Plane and Tip Visualization

The usual practice of US-guided needle-insertion is to employ 2D US to visualize the needle from its long axis to grasp the global position of the needle and visualize the tip from the needle's short axis to target accurate positions. In order to visualize the relevant cross-section of the volume on the long needle axis, coordinates of the plane containing the needle and perpendicular to the ground plane are calculated.

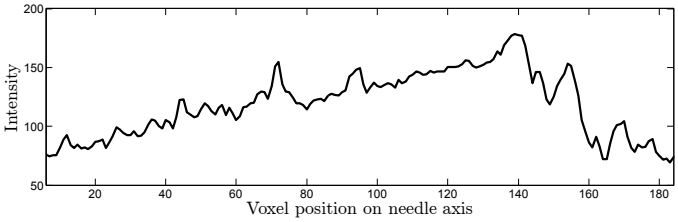

(a) Interpolated intensity of the volume over needle's axis

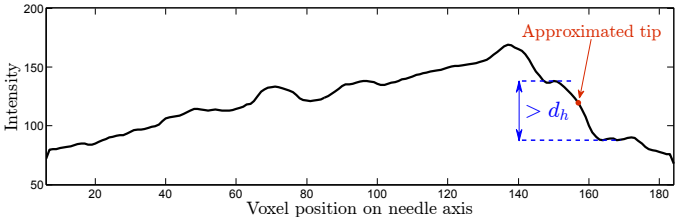

(b) Outcome of moving average on the interpolated signal

Figure 5: Example of needle tip approximation technique

For the short axis, the position of the tip of the needle is approximated to calculate the relevant plane visualization.

The Needle tip is approximated using the hill-climbing technique in the interpolated intensities of the voxels over needle axis. Interpolation is performed by first averaging the intensities in $n_{cs} \times n_{cs}$ pixel cross-sections of the volume at each voxel belonging to the needle axis. Next, a moving average of window size w_f smooths the interpolated signal. The needle tip is then detected when the difference of a local maximum and its corresponding minimum is larger than d_h (see Figure 5).

While the needle orientation and position inside the 3D US volume is known, the coordinates of the planes to best visualize the needle and its tip are calculated as:

$$\begin{aligned} &\text{Long Axis}: (x - x_0)\cos\theta + y\sin\theta = 0, \\ &\text{Short Axis}: (x - (x_0 + l_x))\sin\theta - (y - l_y)\cos\theta = 0, \end{aligned} \tag{10}$$

where $l_x = -(L + n \times dl)\sin\theta$, $l_y = (L + n \times dl)\cos\theta$, L is the approximate length of the needle, dl is the distance between the two subsequent cross-sections and n is the number of required cross sections in the short axis.

IV. Experimental Results

The proposed needle detection algorithm is evaluated on 32 Three-Dimensional Ultrasound (3D US) volumes. Our dataset is created by flipping 8 different 3D US volumes in x and y directions, which were acquired from a chicken breast phantom in 3D with two types of needles and different insertion angles. Spatial resolution of each volume is $160 \times 188 \times 116$ voxels where each voxel is representing $0.17\,\mathrm{mm}^3$. Evaluation is performed for the two developed techniques. The ground-truth Groups of Voxels (GV) are annotated manually for each volume. This is done by finding the two ends of the needle and fitting a needle model in the volume, which is a line with specified length, width and orientation. For the Gabor-based needle detection, voxel-wise detection is evaluated based

Table II: Recall-precision results for voxel-wise detection (%)

GV Size	Needle Type	$w_s = 1$		$w_s = 3$		$w_s = 5$		$w_s = 7$		$w_s = 9$	
		Recall	Precision	Recall	Precision	Recall	Precision	Recall	Precision	Recall	Precision
4	Low-reflective	24.13*	86.78*	47.51*	83.90*	67.11	72.46	54.68	59.00	61.69	56.86
	High-reflective	25.15*	41.58*	46.33	58.78	65.36	61.71	65.59	51.16	51.00	37.34
6	Low-reflective	21.61*	89.49*	36.21	92.01	53.24	86.15	57.06	79.30	51.17	70.18
	High-reflective	30.66*	75.00*	31.01	73.61	48.27	71.90	55.01	70.14	51.13	62.60
8	Low-reflective	8.04*	75.97*	23.21	83.60	31.47	77.12	42.22	79.96	38.93	70.95
	High-reflective	30.38*	88.89*	33.41*	90.92*	36.51	77.06	48.67	80.62	47.39	72.09

* Unable to detect the needle in one or more volumes

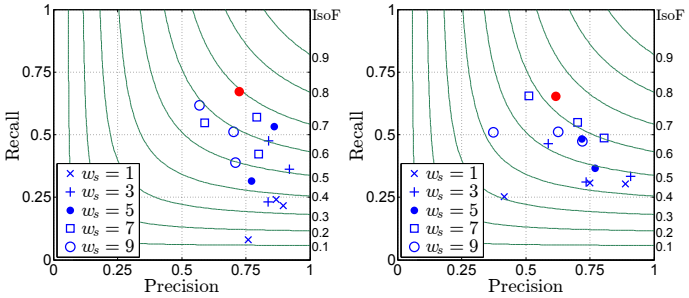

(a) Low-reflective needle (b) High-reflective needle

Figure 6: Voxel detection recall-precision performance

on leave-one-out cross-validation. Accuracy of detecting the needle position and its 3D orientation is evaluated for both detection techniques. Performance of the needle tracking algorithm is evaluated assuming a position of the needle in the previous moment of time. Furthermore, the performance of the proposed algorithm to detect and visualize the needle and its tip with 2D cross-sections of the volume is assessed visually.

In our implementation, we use the following parameters: two successions of spatial median filter of 3×3 pixels, $d_b = 4$, $\epsilon = 2.5$ and $n_{cs} = 4$.

A. Voxel-wise Detection Evaluation

As the aim of this study is to find 2D cross-sections of 3D volumes that need to be visualized to the operator, evaluation at the voxel level cannot completely reflect the performance of the algorithm. However, in order to obtain an objective measure of how adjusting detection parameters can influence accuracy and reliability of the algorithm, we employ recall and precision metrics and proceed as follows. A True Positive (TP) is counted when a detected GV is found on the ground-truth. A detected GV that has no match in ground truth, counts as a False Positive (FP). Finally, a ground-truth GV that is not detected counts as a False Negative (FN). These metrics are measured for all 3D US volumes to calculate recall and precision as follows:

$$\text{Recall} = TP/\left(TP + FN\right), \tag{11a}$$

$$\text{Precision} = TP/\left(TP + FP\right). \tag{11b}$$

Table II shows the recall-precision performances for the voxel-wise detection stage for different GV sizes and Gabor complex-cell sub-sampling size w_s. Some parameter choices

Table III: Evaluation of needle detection algorithms*

Method	Needle Type	Fails	ε_p	ε_θ	ε_ϕ
Projection based	Low-reflective	75%	1.86 mm	1.79°	1.59°
	High-reflective	75%	0.41 mm	1.03°	0.69°
Gabor based	Low-reflective	0%	1.18 mm	2.97°	1.06°
	High-reflective	0%	2.40 mm	6.67°	1.41°
Gabor based + Gradient Descent	Low-reflective	0%	0.76 mm	2.13°	0.56°
	High-reflective	0%	1.20 mm	3.27°	1.22°

* Length of the needle in the volume is at least 1 cm

cause the detection algorithm to fail in one or more of the volumes, which are indicated with a (*) appended to the performance score. Since high Gabor responses belonging to the needle are dominant, increasing the spatial sub-sampling size increases the number of adjacent voxels that are represented by needle's responses. Therefore, as shown in Table II, with increasing w_s, TP and FP are increased, which causes a lower precision and higher recall.

Figure 6 shows the recall-precision performance for different detection parameters. Harmonic mean of recall and precision, also known as the F-measure, is used to find the best performance. The red dot represents the highest F-measure, which is for $w_s = 5$ and a GV size of 4 voxels. Moreover, it can be derived that the best performance for each w_s corresponds to the closest GV size. The poor performance for the high-reflective needle can be explained by the increased illumination variations for different insertion angles.

B. Needle Detection Evaluation

The overall performance of the needle detection algorithm is evaluated by introducing position and orientation errors. The needle position error (ε_p) is calculated as the average of the Euclidean distances between each point of the detected needle and the ground-truth. Also the errors ε_θ and ε_ϕ in the detected azimuth and elevation angles of needle, respectively, are calculated as the orientation errors. Table III shows the performance evaluation of the projection-based and Gabor-based needle detection algorithms. Detection parameters are chosen for the best recall-precision performance.

The results from Table III show that, although the projection-based technique detects the needle with the lowest errors, it fails in 75% of the dataset. Depending on needle orientation and visibility in the volume, projection may obscure parts or the whole needle, which makes detection difficult or even impossible. However, with the Gabor-based technique, the local structure of the needle in 3D is employed,

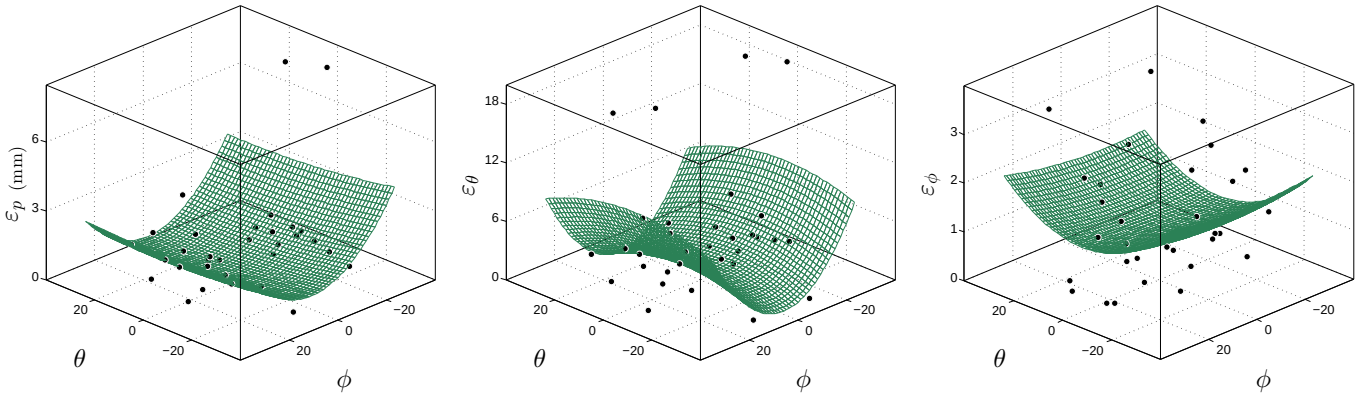

(a) Needle position error (b) Azimuth angle error (c) Elevation angle error

Figure 7: Gabor-based needle detection error as function of needle azimuth and elevation angles

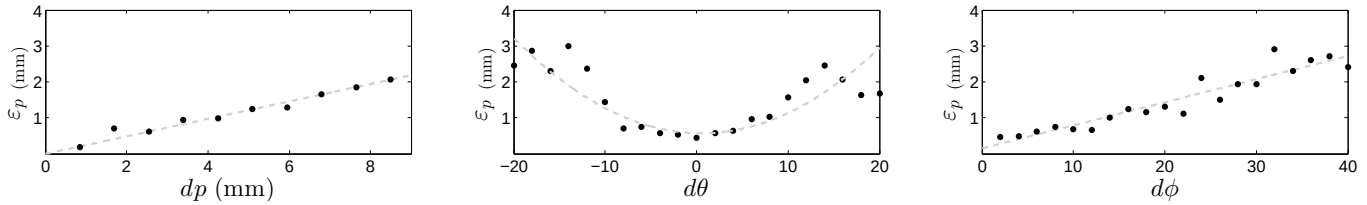

(a) Needle position error vs. needle axis movement (b) Needle position error vs. needle azimuth angle movement (c) Tracking stage needle position error vs. needle elevation angle movement

Figure 8: Needle tracking error for different needle movements

which clearly improves the success rate. However, due to the spatial sub-sampling of Gabor transformation, the accuracy of detection is penalized. Utilizing the gradient descent search of the tracking stage to locally adjust the position and orientation, decreases the errors nearly by a factor of two and preserves the success rate at 100%.

Figure 7 shows the Gabor-based position and orientation errors. In order to examine the relation of errors with needle azimuth and elevation angles, second-order curves are fitted on the data. As shown, the needle position and azimuth errors increase for steeper needles. However, variations of the needle azimuth angle does not have large influence on the error. The four large azimuth errors are introduced by flipped versions of one volume, in which the RANSAC algorithm is misled by a miss-classified region. On the other hand, the elevation angle error is very small compared to the other two errors and varies slowly for different needle insertion angles.

C. Needle Tracking Evaluation

The performance of the needle-tracking stage is evaluated on pseudo sequences of 3D US data, which is constructed by assuming a position of the needle in the previous moment of time. The ability of the algorithm to track the needle is shown in Figure 8. The average of the position error (ε_p) is calculated on the whole dataset for different movements of the needle in position, azimuth angle and elevation angle. As shown, the tracking algorithm is able to accurately find back the needle for small movements and the error grows as the needle movement increases. However, it should be noted that needle movements of more than $4\,\mathrm{mm}$ in position and 20 degrees in angle are not realistic in US-guided needle interventions.

The computational complexity of the tracking stage depends on the needle movement and increases with larger movements. The average processing time of tracking varies between $383\,\mathrm{ms}$ to $1163\,\mathrm{ms}$ for the MATLAB implementation on a 2.4-GHz Core i5-520M laptop computer.

D. Visual Evaluation

The objective of the proposed algorithm is to visualize the cross-section of the volume, which contains the full-length needle. Figure 9 shows examples of planes detected and visualized by the algorithm in comparison with the ground-truth needle planes. The first two columns at the left are from low-reflective needles and the second two columns are cross-sections from high-reflective needles. The most-right cross-section shows the largest detection error, which is caused by the needle-like bright region under the tip of the needle.

Moreover, cross-sections of the volume from the needle's short-axis are visualized to the operator. Examples of the short-axis visualization are shown in Figure 10. As shown, the fifth cross-section perpendicular to needle's axis contains the approximate position of tip of the needle in its center. Preceding and succeeding cross-sections with relation to cross-section 5 visualize approaching and approached structures (or vice versa) to the operator, which assists for detecting the target and navigating the needle.

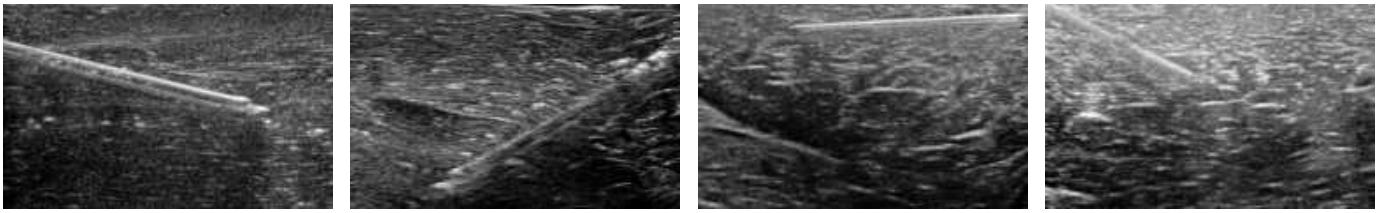

(a) Ground-truth needle planes

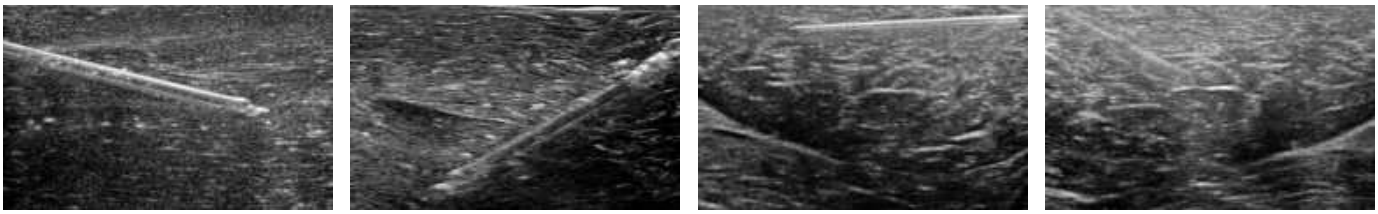

(b) Detected needle planes

Figure 9: Comparison of the detected and the ground-truth needle planes

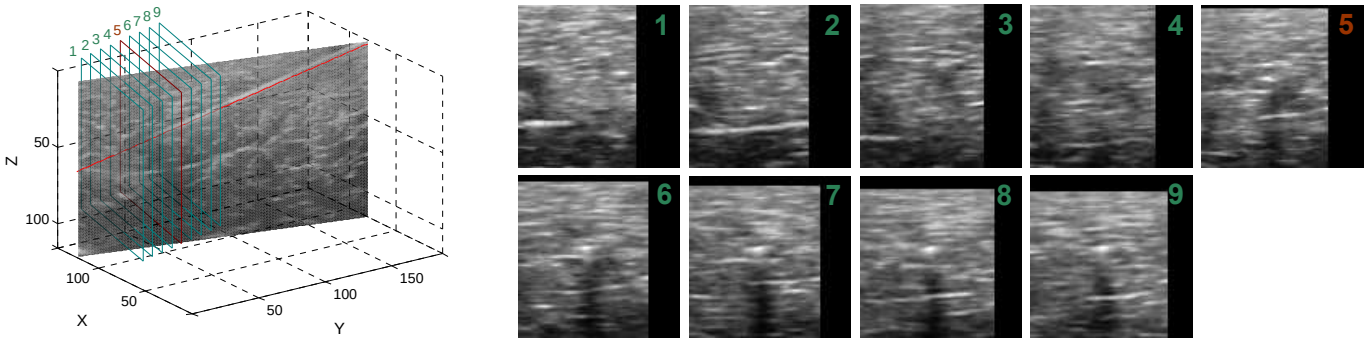

Figure 10: Example of short-axis visualization: left – arrangements of the needle axis, long-axis visualization and short axis visualization planes in 3D, right – short-axis visualization planes, tip of the needle is visible from 5-9 as a bright spot in the middle of the image, images 2-4 do not contain the needle

V. Conclusions and Future Work

In this work, we have proposed a novel needle detection algorithm for three-dimensional Ultrasound (3D US) imaging, which visualizes 2D cross-sections of the needle and its tip with respect to the local structures. The proposed method is based on an efficient image processing concept without employing any external tracking devices, modifications of the acquisition system or the needle itself. The proposed technique involves a normalization method to minimize the variations of needle visibility caused by anisotropic US image formation. Needle detection is performed based on supervised model-based detection, employing a 3D Gabor transformation as a feature extractor, which exploits needle-like structures in the volume. A linear model is fitted to the detected voxels robustly using RANdom SAmple Consecsus (RANSAC) [44]. We have shown the application of our algorithm by visualizing the most relevant 2D cross-sections of the 3D US, which aids the operator to see the needle and its tip with respect to important structures with minimum effort.

We have investigated two different approaches to detect the needle in 3D US volume. First, we have implemented the projection-based detection technique, which has been investigated earlier, easy to implement and is shown to be relatively accurate. However, the earlier studies mainly address non-realistic situations, where the needle is the only bright object in the volume. We have shown that in ex-vivo situations, projection-based needle detection fails in about 75% of the trials. The other proposed approach is based on the 3D Gabor transformation, in which we employ a discriminative model of the needle to be verified inside the 3D US volume. We have evaluated our proposed technique on 32 volumes and have shown the high success rate of detecting the needle and high accuracy of visualizing the needle and its tip.

Future work should focus on detecting shorter needles to increase the reliability of the algorithm. More extensive evaluation enables the best choice of Gabor transformation parameters. Work should also be done on acquiring 3D US volumes of needle intervention on patients and clinically evaluating the algorithms. Furthermore, the real-time implementation of the algorithm will enable the proposed technique to be set up in parallel to the acquisition system for live intervention support. Our study has proved the feasibility of image-analysis-based needle detection for 3D US.

REFERENCES

[1] B. U. Karbeyaz and N. G. Gençer, "Electrical conductivity imaging via contactless measurements: an experimental study," *IEEE transactions on Medical Imaging*, vol. 22, no. 5, pp. 627–35, 2003.

[2] C. Papalazarou, P. J. Rongen, and P. H. N. de With, "Surgical needle reconstruction using small-angle multi-view X-ray," in *IEEE International Conf. on Image Processing (ICIP)*, 2010, pp. 4193–6.

[3] B. Yusupov and S. Zlochiver, "Biopsy needle localization using magnetic induction imaging principles: a feasibility study." *IEEE transactions on Biomedical Engineering*, vol. 59, no. 8, pp. 2330–7, 2012.

[4] J. W. Cannon, J. A. Stoll, I. S. Salgo, H. B. Knowles, R. D. Howe, P. E. Dupont, G. R. Marx, and P. J. del Nido, "Real Time 3-Dimensional Ultrasound for Guiding Surgical Tasks," *Computer Aided Surgery*, vol. 8, no. 2, pp. 82–90, 2003.

[5] K. J. Draper, C. C. Blake, L. Gowman, D. B. Downey, and A. Fenster, "An algorithm for automatic needle localization in ultrasound-guided breast biopsies," *Medical Physics*, vol. 27, no. 8, pp. 1971–9, 2000.

[6] Z. Wei, L. Gardi, D. B. Downey, and A. Fenster, "Oblique needle segmentation for 3D TRUS-guided robot-aided transperineal prostate brachytherapy," in *IEEE International Symposium on Biomedical Imaging (ISBI)*, 2004, pp. 960–3.

[7] D. F. Leotta, "An efficient calibration method for freehand 3-D ultrasound imaging systems," *Ultrasound in Medicine & Biology*, vol. 30, no. 7, pp. 999–1008, 2004.

[8] F. Lindseth, G. A. Tangen, T. Langø, and J. Bang, "Probe calibration for freehand 3-D ultrasound," *Ultrasound in Medicine & Biology*, vol. 29, no. 11, pp. 1607–23, 2003.

[9] S. Cheung and R. N. Rohling, "Enhancement of needle visibility in ultrasound-guided percutaneous procedures," *Ultrasound in Medicine & Biology*, vol. 30, no. 5, pp. 617–24, 2004.

[10] J. William, C. C. Reading, and J. Welch, "CT and sonographically guided needle biopsy: current techniques and new innovations," *American Journal of Roentgenology*, vol. 154, no. 1, pp. 1–10, 1990.

[11] J. L. Prince and J. M. Links, *Medical Imaging Signals And Systems*, Pearson Prentice Hall, 2006.

[12] S. H. Contreras Ortiz, T. Chiu, and M. D. Fox, "Ultrasound image enhancement: A review," *Biomedical Signal Processing and Control*, vol. 7, no. 5, pp. 419–28, 2012.

[13] U. R. Abeyratne, A. P. Petropulu, and J. M. Reid, "Higher order spectra based deconvolution of ultrasound images," *IEEE Transactions on Ultrasonics, Ferroelectrics and Frequency Control (T-UFFC)*, vol. 42, no. 6, pp. 1064–75, 1995.

[14] Y. Chen, R. Yin, P. Flynn, and S. Broschat, "Aggressive region growing for speckle reduction in ultrasound images," *Pattern Recognition Letters*, vol. 24, no. 4-5, pp. 677–91, 2003.

[15] P. Perona and J. Malik, "Scale-space and edge detection using anisotropic diffusion," *IEEE Transactions on Pattern Analysis and Machine Intelligence (TPAMI)*, vol. 12, no. 7, pp. 629–39, 1990.

[16] C. P. Loizou, C. S. Pattichis, C. I. Christodoulou, R. S. H. Istepanian, M. Pantziaris, and A. Nicolaides, "Comparative evaluation of despeckle filtering in ultrasound imaging of the carotid artery," *IEEE Transactions on Ultrasonics, Ferroelectrics and Frequency Control (T-UFFC)*, vol. 52, no. 10, pp. 1653–69, 2005.

[17] R. G. Dantas and E. T. Costa, "Ultrasound Speckle Reduction Using Modified Gabor Filters," *IEEE Transactions on Ultrasonics, Ferroelectrics and Frequency Control (T-UFFC)*, vol. 54, no. 3, pp. 530–8, 2007.

[18] X. Zong, A. F. Laine, and E. A. Geiser, "Speckle reduction and contrast enhancement of echocardiograms via multiscale nonlinear processing," *IEEE Transactions on Medical Imaging*, vol. 17, no. 4, pp. 532–40, 1998.

[19] S. Finn, M. Glavin, and E. Jones, "Echocardiographic speckle reduction comparison," *IEEE Transactions on Ultrasonics, Ferroelectrics and Frequency Control (T-UFFC)*, vol. 58, no. 1, pp. 82–101, 2011.

[20] K. Krissian, C.-F. Westin, R. Kikinis, and K. G. Vosburgh, "Oriented Speckle Reducing Anisotropic Diffusion," *IEEE Transactions on Image Processing*, vol. 16, no. 5, pp. 1412–24, 2007.

[21] R. Ebrahimi, S. H. Okazawa, R. N. Rohling, and S. E. Salcudean, "Hand-Held Steerable Needle Device," in *Medical Image Computing and Computer-Assisted Intervention (MICCAI)*, 2003, pp. 223–30.

[22] S. H. Okazawa, R. Ebrahimi, J. Chuang, R. N. Rohling, and S. E. Salcudean, "Methods for segmenting curved needles in ultrasound images," *Medical Image Analysis*, vol. 10, no. 3, pp. 330–42, 2006.

[23] M. Aboofazeli, P. Abolmaesumi, P. Mousavi, and G. Fichtinger, "A New Scheme for Curved Needle Segmentation in Three-Dimensional Ultrasound Images," in *IEEE International Symposium on Biomedical Imaging (ISBI)*, 2009, pp. 1067–70.

[24] A. Ayvaci, P. Yan, S. Xu, S. Soatto, and J. Kruecker, "Biopsy needle detection in transrectal ultrasound," *Computerized Medical Imaging and Graphics*, vol. 35, no. 7-8, pp. 653–9, 2011.

[25] H. R. S. Neshat and R. V. Patel, "Real-time parametric curved needle segmentation in 3D ultrasound images," in *IEEE/RAS-EMBS International Conf. on Biomedical Robotics and Biomechatronics (BioRob)*, 2008, pp. 670–5.

[26] M. Ding and A. Fenster, "Projection-based needle segmentation in 3D ultrasound images," *Computer Aided Surgery*, vol. 9, no. 5, pp. 193–201, 2004.

[27] H. Zhou, W. Qiu, M. Ding, and S. Zhang, "Automatic needle segmentation in 3D ultrasound images using 3D improved Hough transform," in *Proc. SPIE 6918, Medical Imaging: Visualization, Image-guided Procedures, and Modeling, 691821*, 2008.

[28] W. Qiu, M. Ding, and M. Yuchi, "Needle Segmentation Using 3D Quick Randomized Hough Transform," in *International Conf. on Intelligent Networks and Intelligent Systems (ICINIS)*, 2008, pp. 449–52.

[29] P. Yan, J. C. Cheeseborough, and K. S. C. Chao, "Automatic shape-based level set segmentation for needle tracking in 3-D TRUS-guided prostate brachytherapy," *Ultrasound in medicine & biology*, vol. 38, no. 9, pp. 1626–36, 2012.

[30] M. Ding, H. N. Cardinal, and A. Fenster, "Automatic needle segmentation in 3D ultrasound images using two orthogonal 2D image projections," *Medical Physics*, vol. 30, no. 2, pp. 222–34, 2003.

[31] Z. Wei, L. Gardi, D. B. Downey, and A. Fenster, "Oblique needle segmentation and tracking for 3D TRUS guided prostate brachytherapy," *Medical Physics*, vol. 32, no. 9, pp. 2928–41, 2005.

[32] P. Hartmann, M. Baumhauer, J. Rassweiler, and H. P. Meinzer, "Automatic Needle Segmentation in 3D Ultrasound Data Using a Hough Transform Approach," in *Bildverarbeitung für die Medizin*, 2009, pp. 341–5.

[33] M. Barva, J. Kybic, J.-M. Mari, C. Cachard, and V. Hlavac, "Automatic localization of curvilinear object in 3D ultrasound images," in *Proc. SPIE 5750, Medical Imaging: Ultrasonic Imaging and Signal Processing, 455*, 2005.

[34] M. Uhercík, J. Kybic, H. Liebgott, and C. Cachard, "Model fitting using RANSAC for surgical tool localization in 3D ultrasound images," *IEEE Transactions on Biomedical Engineering*, vol. 57, no. 8, pp. 1907–16, 2010.

[35] F. Gaufillet, H. Liebgott, M. Uhercík, F. Cervenansky, J. Kybic, and C. Cachard, "3D Ultrasound real-time monitoring of surgical tools," in *IEEE International Ultrasonics Symposium (IUS)*, 2010, pp. 2360–3.

[36] Y. Zhao, H. Liebgott, and C. Cachard, "Tracking micro tool in a dynamic 3D ultrasound situation using Kalman filter and RANSAC algorithm," in *IEEE International Symposium on Biomedical Imaging (ISBI)*, 2012, pp. 1076–9.

[37] M. Uhercík, J. Kybic, C. Cachard, and H. Liebgott, "Line filtering for detection of microtools in 3D ultrasound data," in *IEEE International Ultrasonics Symposium (IUS)*, 2009, pp. 594–97.

[38] B. Dong, E. Savitsky, and S. Osher, "A Novel Method for Enhanced Needle Localization Using Ultrasound-Guidance," in *Proceedings of the International Symposium on Advances in Visual Computing (ISVC)*, 2009, pp. 914–23.

[39] M. Ding and A. Fenster, "A real-time biopsy needle segmentation technique using Hough Transform," *Medical Physics*, vol. 30, no. 8, pp. 2222–33, 2003.

[40] K. S. Roberts, "A new representation for a line," in *IEEE Conf. on Vision and Pattern Recognition (CVPR)*, 1988, pp. 635–40.

[41] S. Helgason, *The Radon Transform*, 2nd ed., Boston, MA: Birkhauser, 1999.

[42] P. M. Novotny, J. A. Stoll, N. V. Vasilyev, P. J. del Nido, P. E. Dupont, T. E. Zickler, and R. D. Howe, "GPU based real-time instrument tracking with three-dimensional ultrasound," *Medical Image Analysis*, vol. 11, no. 5, pp. 458–64, 2007.

[43] M. Barva, M. Uhercík, J.-M. Mari, J. Kybic, J.-R. Duhamel, H. Liebgott, V. Hlavac, and C. Cachard, "Parallel Integral Projection Transform for Straight Electrode Localization in 3-D Ultrasound Images," *IEEE Transactions on Ultrasonics, Ferroelectrics and Frequency Control (T-UFFC)*, vol. 55, no. 7, pp. 1559–69, 2008.

[44] M. A. Fischler and R. C. Bolles, "Random sample consensus: a paradigm for model fitting with applications to image analysis," *Communications of the ACM (CACM)*, vol. 24, no. 6, pp. 381–95, 1981.

[45] H. H. M. Korsten, P. H. N. de With, and J. W. M. Bergmans, "Needle detection in medical image data," U.S. Patent 0 321 154 A1, 2012.

[46] I. Schafhalter-Zoppoth, C. E. McCulloch, and A. T. Gray, "Ultrasound visibility of needles used for regional nerve block: An in vitro study," *Regional Anesthesia and Pain Medicine*, vol. 29, no. 5, pp. 480–8, 2004.
[47] S. D. Cvetkovic, "Optimization of video capturing and tone mapping in video camera systems," Ph.D. dissertation, Technische Universiteit Eindhoven, 2011.
[48] J. P. Jones and L. A. Palmer, "An evaluation of the two-dimensional Gabor filter model of simple receptive fields in cat striate cortex," *Journal of neurophysiology*, vol. 58, no. 6, pp. 1233–58, 1987.
[49] J.-K. Kamarainen, V. Kyrki, and H. Kalviainen, "Noise tolerant object recognition using Gabor filtering," in *International Conf. on Digital Signal Processing*, 2002, pp. 1349–52.
[50] ——, "Fundamental frequency Gabor filters for object recognition," in *International Conf. on Pattern Recognition*, 2002, pp. 628–31.
[51] T. Serre, L. Wolf, S. Bileschi, M. Riesenhuber, and T. Poggio, "Robust object recognition with cortex-like mechanisms," *IEEE Transactions on Pattern Analysis and Machine Intelligence (TPAMI)*, vol. 29, no. 3, pp. 411–26, 2007.
[52] I. T. Young and L. J. van Vliet, "Recursive implementation of the Gaussian filter," *Signal Processing*, vol. 44, no. 2, pp. 139–51, 1995.
[53] I. T. Young, L. J. van Vliet, and M. van Ginkel, "Recursive Gabor Filtering," *IEEE Transactions on Signal Processing*, vol. 50, no. 11, pp. 2798–805, 2002.
[54] A. Bernardino and J. Santos-Victor, "Fast IIR isotropic 2-D complex Gabor filters with boundary initialization," *IEEE Transactions on Image Processing*, vol. 15, no. 11, pp. 3338–48, 2006.
[55] J.-M. Geusebroek, A. W. M. Smeulders, and J. van de Weijer, "Fast anisotropic Gauss filtering," *IEEE Transactions on Image Processing*, vol. 12, no. 8, pp. 938–43, 2003.
[56] G. Amayeh, A. Tavakkoli, and G. Bebis, "Accurate and Efficient Computation of Gabor Features in Real-Time Applications," in *International Symposium on Advances in Visual Computing*, 2009, pp. 243–52.

APPENDIX

A. Gabor Transformation Complexity

In order to extract features with Gabor transformation, a bank of Gabor filters should be implemented containing different orientation sensitive filters to be applied to the 3D volume. Performing multiple time the three-dimensional filtering requires a high amount of computing resources and memory. It is worth noting that in a sequence of 3D US volumes, Gabor-transformation-based needle detection can provide the approximate position and orientation of the needle, and therefore sufficient to be performed at selected frames only. However, in order to decrease the computational complexity of the transformation, approaches are proposed in the literature summarized in Table IV.

1) Filtering in the Fourier Domain: Filtering which is a 2D or 3D convolution in the spatial domain is transformed to inner product in the Fourier domain:

$$r_{\xi}(x,y,z) = \mathcal{F}^{-1}\left[\hat{g}(u,v,w).\hat{\xi}(u,v,w)\right]. \qquad (12)$$

For this purpose, Fast Fourier Transforms (FFT) of the filter bank and of the volume to be analyzed, followed by the Inverse FFT (IFFT) of the response of each filter. Constructing the filter bank in the Fourier domain can be done offline. However, IFFT of each filter's response in the Fourier domain needs to be calculated, which limits the filtering speed.

2) Recursive Filtering: A fast implementation of convolution of a signal with discrete Gaussian is proposed through concatenation of two recursive filters [52], which consists of 7 real multiplication and 6 real additions per pixel per dimension. A recursive 1D Gabor filter proposed in the follow-up study [53], multiplies the Gaussian weights with complex exponential and therefore consists of 7 complex multiplication and 6 complex additions. Gabor filtering decomposition to recursive Gaussian filtering following by a multiplication with a complex exponential is proposed for isotropic 2D implementations [54], showing about 30% savings in computation.

3) Separability of Gabor Filters: A filter g can be constructed from a sequence of one dimensional convolutions, if and only if its Fourier transform factorizes [55]:

$$\begin{aligned} g(x,y,z) &= g_x(x) * g_y(y) * g_z(z) \Leftrightarrow \\ \hat{g}(u,v,w) &= \hat{g}_u(u)\,\hat{g}_v(v)\,\hat{g}_w(w). \end{aligned} \qquad (13)$$

The Fourier transform of the 3D Gabor filter factorizes in u_r, v_r and w_r directions. As the separation along the original coordinate system directions is more interesting from a computational prospective, the filter can be separated into two 1D convolutions along the u, v and a third 1D convolution along direction t. The latter convolution implies an interpolation step, which can be integrated in the convolution [56].

Table IV: Complexity per pixel of 3D Gabor filters algorithms

Algorithm	Separability	Complexity	
		Multiplications	Additions
3D convolution	-	NMP	$NMP-1$
FFT convolution	-	$\log WHL$	$\log WHL$
Separated 1D convolutions	xyz^*	$\lfloor N/2\rfloor+\lfloor M/2\rfloor+\lfloor P/2\rfloor+3$	$N+M+P-3$
	$x_ry_rz_r$	$3(N+M+P-1)$	$3(N+M+P-3)$
	xyt	$\lfloor N/2\rfloor+\lfloor M/2\rfloor+M+1$	$N+M+2P-4$
Separated recursive	xyz^*	78	23
	$x_ry_rz_r$	123	53
	xyt	87	33

Filter size is denoted by $N \times M \times P$
Volume size is denoted by $W \times H \times L$
* Restricted to filters with $\theta = k\frac{\pi}{2}$ and $\phi = k'\frac{\pi}{2}$